Chemical Engineering Science 280 (2023) 119084

Contents lists available at ScienceDirect

Chemical Engineering Science

journal homepage: www.elsevier.com/locate/ces

High-throughput synthesis of high-purity and ultra-small iron phosphate nanoparticles by controlled mixing in a chaotic microreactor

Zu-Chun Shi [a,1], Shi-Xiao Wei [a,1], Ting-Liang Xie [a,*], Qiang Liu [a], Chak-Tong Au [b], Shuang-Feng Yin [a,*]

[a] College of Chemistry and Chemical Engineering, Advanced Catalytic Engineering Research Center of the Ministry of Education, State Key Laboratory of Chemo/Biosensing and Chemometrics, Hunan University, Changsha 410082, PR China
[b] College of Chemical Engineering, Fuzhou University, Fuzhou 350002, PR China

ARTICLE INFO

Keywords:
Oscillating feedback microreactor
Chaotic advection
Inlet structures
Iron phosphate nanoparticles
High-throughput

ABSTRACT

High-purity $FePO_4$ with small particle size is pivotal for improving electrochemical performance of $LiFePO_4$-based lithium-ion batteries. Here, an oscillating feedback microreactor (OFM) based on chaotic advection was designed to prepare high-quality $FePO_4$ by coprecipitation. Dye-tracer experiments and CFD simulations were adopted to investigate fluid mixing mechanism and to evaluate mixing efficiency in the reactor. The results indicated that a "flow-focused" OFM (FOFM) performed better than a "Y-junction" OFM in mixing performance, owing to enhanced premixing in focused inlet microchannel of the former. The results of Villermaux-Dushman experiments illustrated that almost complete mixing could be achieved in 0.16 ms in FOFM. Accordingly, $FePO_4$ nanoparticles of good quality was synthesized using FOFM, and the particle size can be easily controlled by adjusting flow rate or reactant concentration. High-purity (P/Fe molar ratio: 0.95–1.04) and ultra-small $FePO_4$ nanoparticles (9 nm) with narrow particle size distribution were generated at a high throughput of 180 mL/min.

1. Introduction

Driven by the prevalence of portable electronic devices and the increasing environment/climate issues, considerable efforts have been devoted to the development of rechargeable lithium-ion batteries (LIBs). Among the advanced cathode materials, olivine lithium iron phosphate ($LiFePO_4$) is emerging as one of the most competitive cathode materials for LIBs due to its low cost, environmental friendliness, good thermal and chemical stability and a flat discharge potential at 3.4 V versus Li/Li^+. (Kumar et al., 2022) However, it was found that the electrochemical performance (such as rate capability) of $LiFePO_4$-based LIBs is limited by two major factors: the low Li-ion diffusion rate and poor electronic conductivity. (Cui et al., 2020; Meng et al., 2022) Various strategies were proposed to overcome the problems. Among them, reducing the size of $LiFePO_4$ to nanoscale was considered to be simple and efficient. For example, Meng et al. reported that the charge transport and the diffusion rate of Li ions were significantly improved when the $LiFePO_4$ crystals was changed from micrometer-sized bulky particles to nanorods. (Meng et al., 2022) In addition, impurities in the structure can have a negative effect on electrochemical performance. It is because even in trace amount the impurities may block the migration channels and cause capacity loss. For example, Xie et al. noted that magnetic impurities of LIBs could reduce both the capacity and cycling rates, which could be detrimental to battery safety. (Xie et al., 2018).

Iron phosphate ($FePO_4$) is an important precursor for $LiFePO_4$ generation. In LIBs industry, the $FePO_4$ crystals must be highly pure in phase, small in size and controllable in particle size distribution (PSD). Traditional industrial methods for preparing $FePO_4$ nanoparticles (NPs) are usually based on batch (Fig. 1a) or semibatch processes, (Park et al., 2022; Cao et al., 2022) which have drawbacks. Due to the poor mass/heat transfer efficiency in batch or semibatch mode, the prepared $FePO_4$ crystals would be large in average size, broad in PSD, non-uniform in morphology, and displaying high quality undulation between different batches. Also, because of the complexity of the multicomponent coprecipitation process, it is difficult to obtain high purity samples from the precipitation of iron (III) salts and phosphates following the batch or

* Corresponding authors.
E-mail addresses: xtl2020041@hnu.edu.cn (T.-L. Xie), sf_yin@hnu.edu.cn (S.-F. Yin).
[1] The authors contributed equally to this work.

https://doi.org/10.1016/j.ces.2023.119084
Received 22 March 2023; Received in revised form 15 June 2023; Accepted 10 July 2023
Available online 13 July 2023

semibatch mode. To be specific, due to the easy hydrolysis of iron (Fe) ions and the uneven concentration field and temperature field in batch or semibatch processes, there is a variety of products, such as $FePO_4$, $Fe_4(P_2O_7)_3$, $Fe_2(HPO_4)_3$, and so on. (Cao et al., 2022) To circumvent these problems and to continuously produce $FePO_4$ NPs of acceptable quality, a reaction environment uniform at molecular level (i.e., uniform both in concentration and temperature field for crystal nucleation and growth) is required for $FePO_4$ precipitation. And this can be achieved by fast and efficient mixing of the reactants. Recently, microreactors have attracted extensive attention in the synthesis of micro/nano particles, owing to the advantages of high heat/mass transfer efficiency and continuous production. (Liu et al., 2022b; Sui et al., 2020; Kong et al., 2019; Fan et al., 2021) The dimension of microereactors is characteristically ranging from tens to hundreds of microns, and the afforded large surface-to-volume ratios and short diffusion lengths enable fast and efficient mass/heat transfer in the microchannels, resulting in effective control of microprecipitation environment for crystal nucleation and growth. (Hakke et al., 2021).

Beside the size and purity issues, the high-yield production of pure $FePO_4$ NPs is another concern owing to the rapid development of $LiFePO_4$-based LIBs. The traditional mciroreactors mainly include lamination flow (Hao et al., 2019) (Fig. 1b) and segmented flow (Zhang et al., 2022) (Fig. 1c and d) modes. For the lamination flow microreactor (Fig. 1b), the fluids usually flow side by side in the microchannel and the mixing efficiency is relatively low because mass transfer is mainly controlled by molecular diffusion owing to thermal motion of molecules. (Zhang et al., 2023; Pekkari et al., 2019) Hence, low flow rates should be adopted to obtain adequate residence time for improving mixing performance. For the segmented flow microreactor (Fig. 1c and 1d), an insoluble liquid phase is usually adopted as dispersed phase to induce a two-phase flow. The mass transfer can be enhanced by the vortex flow inside the dispersed droplets (Fig. 1c) or slugs (Fig. 1d), thus uniform concentration and temperature fields can be generated for crystal nucleation and growth. (Yang et al., 2020; Stolzenburg et al., 2018) However, low flow rates should also be utilized to keep the stability of this fragile flow pattern. In summary, the lamination flow and segmented flow modes cannot meet the demand of high throughput production, because their total flow rates are usually smaller than 10 mL/min. Although scaling up through number-up method can improve the throughput to some extent, it is difficult to guarantee product uniformity across the sub-reactors. Therefore, a high-throughput microreactor should be developed to address these problems.

Different from the lamination and segment microreactors, the oscillating feedback microreactors (OFMs) based on chaotic advection operate at high throughput, and the characteristic dimension of the mixing chamber is at millimetre scale, which can significantly improve the throughput. (Yang et al., 2022) In addition, the unique three secondary flows (i.e., vortex, feedback and oscillation) allow efficient chaotic mixing (i.e., the fluid is constantly stretched, folded and squeezed), which can compensate for the reduced heat/mass transfer owing to the larger size of the mixing chamber, providing uniform concentration and temperature fields for the nucleation and growth of nanoparticles. (Yang et al., 2022; Liu et al., 2022a; Wei et al., 2022) To the best of our knowledge, there is no report on the use of OFM for the preparation of $FePO_4$ NPs, where the multicomponent coprecipitation system is extremely sensitive to the pH of reactants. Moreover, the microscale mixing process in OFM deserves further investigation to figure out the fluid mixing mechanism for the optimization of reactor structure.

To this end, an OFM was developed for high throughput preparation of $FePO_4$ NPs. To optimize the inlet structure, the fluid flow characteristics and mixing efficiency of the OFM were studied by dye-tracer experiments and computational fluid dynamics (CFD) simulations. The microscale mixing performance in OFM was evaluated by Villermaux-Dushman experiments and CFD simulations. The effects of flow rate and reactant concentration on the average particle size and PSD of $FePO_4$ NPs were investigated. High quality product with small average size (9 nm) was prepared at a high throughput of 180 mL/min.

2. Experimental section

2.1. Oscillating feedback microreactor

According to our previous work (Wei et al., 2022), almost complete mixing could be achieved in the second stage of an OFM, and the fluid mixing performance was significantly affected by the inlet structure. In this study, we designed two kinds of two-stage oscillating feedback microreactors, one contains a flow-focused inlet (denoted herein as FOFM, Fig. 2a), while the other has a Y-junction inlet (denoted herein as YOFM, Fig. 2b). Each stage of the OFM mainly consists of a diverging chamber, a splitter, two barriers and two feedback channels. The width of the feedback channel and outlet channel is 0.4 mm and 0.2 mm, respectively. The depth of all channels is 1.0 mm.

To clearly capture the flow field images in the OFM, the reactors were fabricated by transparent poly (methyl methacrylate) (PMMA) plates (supplied by Guanghe Acrylic Sheet Co., Ltd., Shenzhen, China). The details for the fabrication of a complete microreactor including microchannel machining and PMMA plate sealing were described elsewhere. (Wei et al., 2022) The physical photos of the OFMs with different inlet structures were shown in Fig. S2.

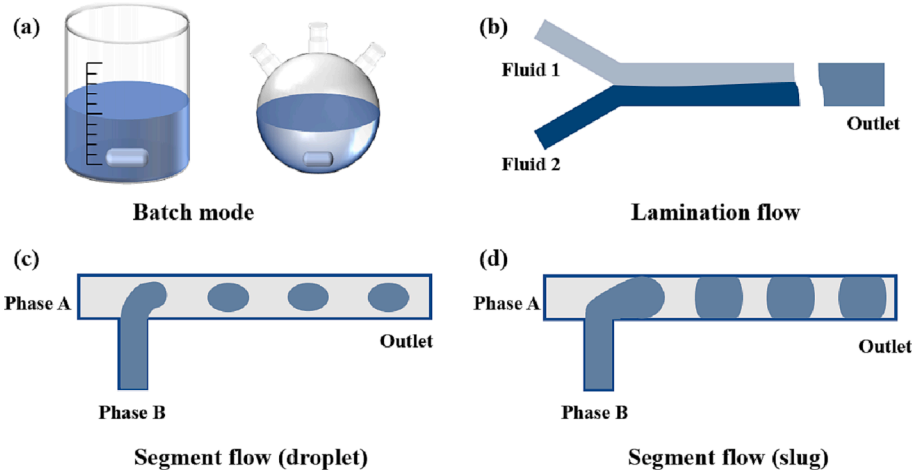

Fig. 1. Four main modes of fluid mixing reactors: (a) batch mode; (b) lamination flow; (c) segment flow (droplet), and (d) segment flow (slug).

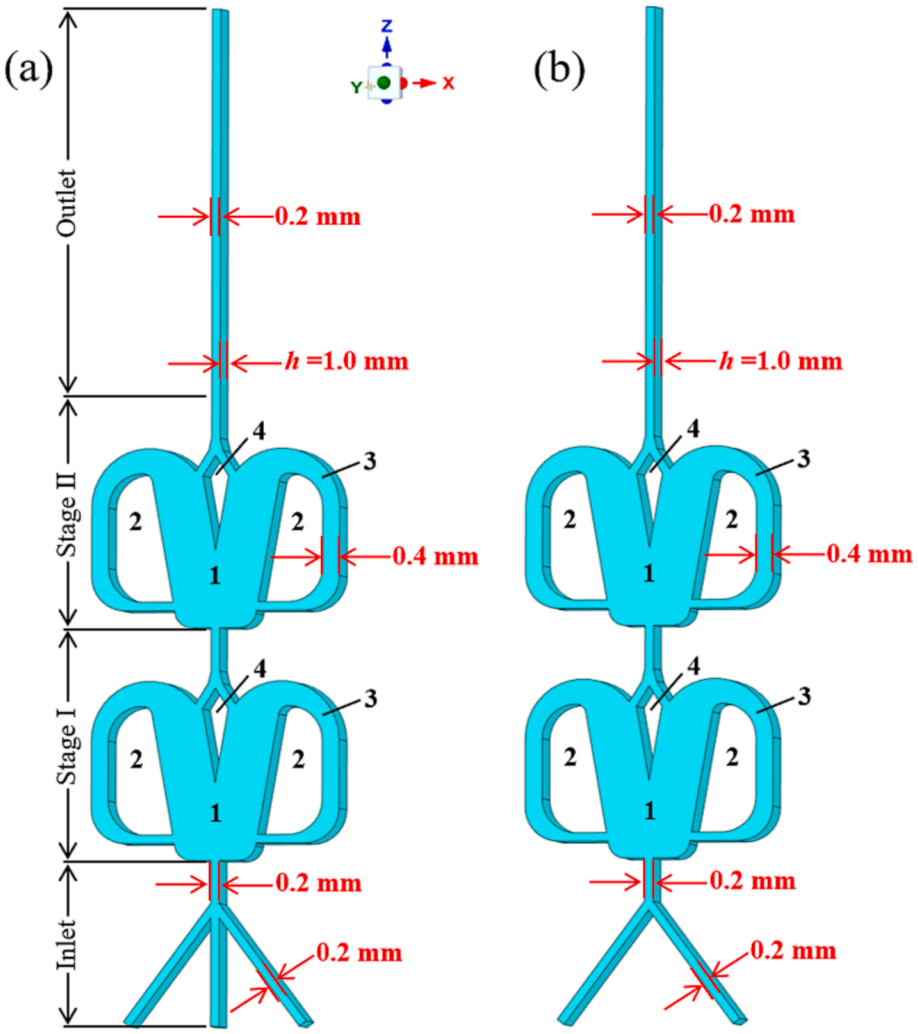

Fig. 2. Structure and dimensions of OFMs with different inlet structures: (a) flow-focused OFM (FOFM), and (b) Y-junction OFM (YOFM). 1: divergent chamber; 2: barrier; 3: feedback channel; 4: splitter.

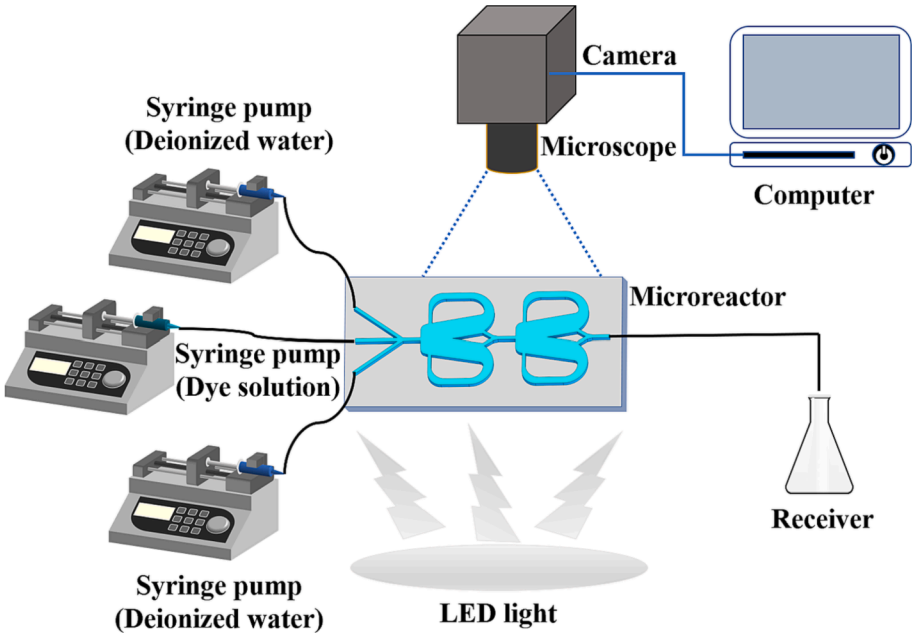

Fig. 3. Schematic of the dye-tracer experiment.

2.2. Chemicals

Brilliant blue, boric acid (H_3BO_3, AR), potassium iodide (KI, AR), potassium iodate (KIO_3, AR), sodium hydroxide (NaOH, AR), sulfuric acid (H_2SO_4, AR), ferric nitrate nonahydrate ($Fe(NO_3)\bullet 9H_2O$, AR), ammonium dihydrogen phosphate ($(NH_4)_2HPO_4$, AR), phosphoric acid (H_3PO_4, AR) and ammonium hydroxide ($NH_3{\cdot}H_2O$, AR) were purchased from Sinopharm Chemical Reagent Co., Ltd. (Shanghai, China). All chemicals were used as received without any further purification. Deionized (DI, 18 MΩ cm) water was used in all experiments.

2.3. Dye-tracer experiment

To explore the influence of reactor inlet structure on fluid mixing and to reveal the flow pattern evolution mechanism in OFM, dye-tracer experiments were conducted. An aqueous solution containing brilliant blue (1 g/300 g H_2O) was used as the color phase, and DI water as the blank phase. For the FOFM, the color phase entered the mixing chamber from the middle channel of the inlet, while the blank phase from the side inlets. With respect to the YOFM, the color phase flowed into the mixing chamber from the left inlet, while the blank phase from the right inlet. The flow rate ratio R_f of the color phase to the blank phase was kept at 1.0. As shown in Fig. 3, three precise syringe pumps (LSP01-1BH, stroke resolution 0.156 μm, Baoding Longer Precision Pump Co., Ltd., Baoding, China) were used to pump the fluids into the mixing chamber at ambient temperature (24±1 °C). A high-definition CCD camera (Canon, EOS M50 Mark II) mounted on a microscope (Ningbo Ankuan Trade Co. Ltd, SZN745TR) was utilized to capture the real images of flow field. A LED light (Shanghai J&K Photoelectronic System Co., Ltd, JK-B100100W-F) was adopted to enhance the recording sharpness.

To quantify the mixing performance in OFMs, the digital images obtained from the flow pattern experiments were processed by using the commercial software MATLAB. The mixing index (*MI*) was utilized to describe the mixing efficiency, and it was defined as follows: (Xu and Chu, 2015)

$$MI = \frac{\sigma_{max} - \sigma}{\sigma_{max} - \sigma_{min}} \tag{1}$$

$$\sigma = \sqrt{\frac{1}{N}\sum_{i=1}^{N}\left(I_{i,n} - \overline{I_{i,n}}\right)^2} \tag{2}$$

$$I_{i,n} = \frac{I_{max} - I_i}{I_{max} - I_{min}} \tag{3}$$

where I_i is the gray scale value (between 0 and 255) of pixel i in the interest region in OFMs. $I_{i,n}$ is the normalized gray scale level for the I_i, and $\overline{I_{i,n}}$ is the average value of $I_{i,n}$. I_{max} and I_{min} are the maximum and minimum gray scale level, respectively. σ notes the standard deviation of the gray value in the selected region, and N is the number of sample points. Noted that the mixing index *MI* ranges from 0 to 1, and the larger the value is, the better the mixing performance is.

2.4. Villermaux – Dushman method

Because of the limited spatial resolution of the optical microscopy, the flow visualization experiments could only provide macroscale/mesoscale mixing information. To obtain mixing properties at microscale, Villermaux–Dushman experimental method based on a parallel competitive reaction was used to quantify the micromixing process in FOFM. The method has been widely used to investigate the microscale mixing performance of microreactors. (Asano et al., 2023; Gaddem et al., 2022; Yang et al., 2021) The Villermaux–Dushman reaction system (Fig. 4) consists of one neutralization reaction, one redox reaction, as well as one reversible reaction, and the specific description of the reaction system is as follows:

$$H_2BO_3^- + H^+ \rightarrow H_2BO_3 (quasi - instantaneous) \tag{4}$$

$$5I^- + IO_3^- + 6H^+ \rightarrow 3H_2O (very fast) \tag{5}$$

$$I_2 + I^- \leftrightarrow I_3^- (instantaneous equilibrium reaction) \tag{6}$$

The neutralization reaction (4) of $H_2BO_3^-$ ions with H^+ ions occurs quasi-instantaneously, and the redox reaction (5) is fast but much slower than that of reaction (4). When the two fluids are completely mixed, the $H_2BO_3^-$ ions would consume all the H^+ ions instantaneously through reaction (4), resulting in the termination of the Dushman reaction (5) owing to the stoichiometric defects of H^+ ions. When the two fluids are partially mixed, the amount of H^+ ions would be greater than that required to neutralize the $H_2BO_3^-$ ions in local area, hence there is a local excess of H^+, resulting in the generation of I_2 and I_3^- ions through reaction (5) and (6), respectively. The concentration of I_3^- ions can be detected by using an on-line UV–Vis detector (UV–Vis-950, Oushisheng (Beijing) Technology Co., Ltd., Beijing, China) at the characteristic wavelength of 350 nm. Consequently, the micromixing efficiency can be measured by using the separation index X_S, which is described as follows:

$$X_S = \frac{Y}{Y_{st}} \tag{7}$$

$$Y = \frac{2V_1\left([I_2] + [I_3^-]\right)}{V_2[H^+]_0} \tag{8}$$

$$Y_{st} = \frac{6[IO_3^-]_0}{6[IO_3^-]_0 + [H_2BO_3^-]_0} \tag{9}$$

The square bracket [] notes the concentration of species, and the

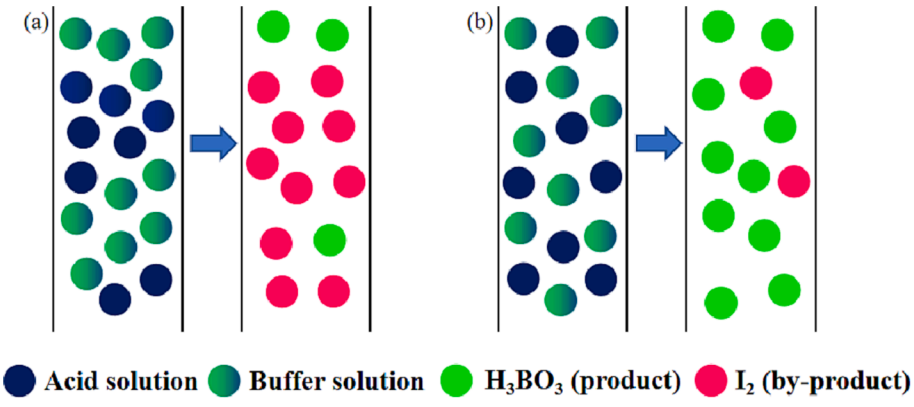

Fig. 4. Schematic of micromixing based on the iodide–iodate reaction system: (a) poorly mixed at molecular scale, (b) well mixed at molecular scale.

subscript 0 denotes the initial state. V_1 is the total volumetric flow rate of H_2SO_4 solution and buffer solution, V_2 represents the volumetric flow rate of H_2SO_4 solution. Y is the ratio of the H^+ consumed in reaction (5) to that of total consumption. Y_{st} represents the value of Y when the mixing is completely separated (i.e., the mixing process is infinitely slow). $X_S = 0$ indicates that the two fluids are completely mixed, while $X_S = 1$ describes that the two fluids are completely separated. As $0 < X_S < 1$, the two fluids are partially mixed, and the smaller the X_S value is, the higher the micromixing efficiency is.

To further describe the mixing process in the FOFM, the separation index was calculated based on the micromixing time (τ_m) by using the incorporation model (Arian and Pauer, 2021a), where sulfuric acid was the limit fluid. For the experiment, the limit fluid could be divided into several aggregates which were continuously invaded by the surrounding alkaline fluids containing iodine and iodate acid. The characteristic time of incorporation is assumed to be equal to τ_m, and the volume growth of the aggregates is illustrated as follows:

$$V_2 = V_{20} g(t) \tag{10}$$

where $V2$ and $V20$ represents the instantaneous volume and initial volume of acid aggregates, respectively, and $g(t)$ notes the volume growth rate function which is defined as follows:

$$g(t) = \exp(t/\tau_m) \tag{11}$$

The concentration (Cj) of species j [illegible] calculated as follows:

$$\frac{dC_j}{dt} = (C_{j10} - C_j)\frac{1}{g}\frac{dg}{dt} + R_j \tag{12}$$

where $Cj10$ is the concentration of j species in the surrounding fluid, and Rj represents the net production rate. After combining equations 11 and 12, equation 13 can be obtained:

$$\frac{dC_j}{dt} = \frac{C_{j10} - C_j}{\tau_m} + R_j \tag{13}$$

It is worth noting that sulfuric acid is a dibasic acid and there is stepwise dissociation, which can be described as follows:

$$H_2SO_4 \rightleftharpoons H^+ + HSO_4^- \tag{14}$$

$$HSO_4^- \rightleftharpoons H^+ + SO_4^{2-} \tag{15}$$

Although the stepwise dissociation does not affect the qualitative analysis of the micromixing, it needs to be considered critically when making quantitative comparisons. (Baqueiro et al., 2018; Guichardon et al., 2021) Therefore, the stepwise dissociation of sulfuric acid was considered when equation (13) was solved using the ODE solver in Matlab, and segregation index X_S could be obtained based on the given τ_m. (Arian and Pauer, 2021b; Arian and Pauer, 2022) The reaction rate constants involved in the calculations are listed in Table S1.

2.5. Synthesis of iron phosphate nanoparticles

The $FePO_4$ samples were synthesized through a coprecipitation method. (Lu et al., 2012; Zhang et al., 2013) First, a certain amount $Fe(NO_3)\bullet 9H_2O$ and $(NH_4)_2HPO_4$ were separately dissolved in DI water for generating the two precursors. Then, the pH values of $Fe(NO_3)\bullet 9H_2O$ solution and $(NH_4)_2HPO_4$ solution were adjusted with H_3PO_4 and $NH_3{\cdot}H_2O$ to form A solution and B solution (Table S2), respectively. Fig. 5 shows the setup for the continuous preparation of $FePO_4$ NPs in the FOFM. Solution A and solution B entered the mixing chamber of reactor from the middle feed channel and the side inlet channels, respectively. The total flow rate Q_{total} was in the range of 10–180 mL/min with a constant flux ratio of 1.0. When the fluid flow was close to the steady state, the precipitate from the outlet was collected in a beaker under continuous stirring. Then, they were transferred into a round-bottom flask for hydrothermal treatment at 110 °C under atmospheric pressure for another 1 h. After this, the product was collected by centrifugation and washed with DI water for three times. Finally, the $FePO_4$ NPs was collected after drying at 60 °C in air for 36 h. For comparison, the coprecipitation process using a batch mode was also conducted as follows: 35 mL solution A (0.1 mol/L) was injected into a beaker containing 35 mL solution B (0.1 mol/L) at a flow rate of 90 mL/min under continuous stirring, then the as-resulted mixed solution was continuously stirred for another minute. The steps that followed were the same as those of $FePO_4$ generation using the the microreactor method.

2.6. Characterization of iron phosphate nanoparticles

The crystal structure of prepared $FePO_4$ NPs was determined by X-ray diffractometry (XRD-6100, Shimadzu, Japan) using Cu Kα radiation (40 KV and 30 mA) at a scanning rate of 8 deg/min after calcination (heated from 30 °C to 800 °C at a rate of 10 °C/min in air). The morphology and size of the samples was determined by field emission Scanning Electron Microscopy (JSM-7610F Plus, JEOL, Japan). Elemental composition (referring to P and Fe) of the product was determined using an inductively coupled plasma–atomic emission spectrometer ICP-AES (Agilent 725, Agilent, America).

3. Simulation section

Despite dye-tracer and Villermaux–Dushman experiments were

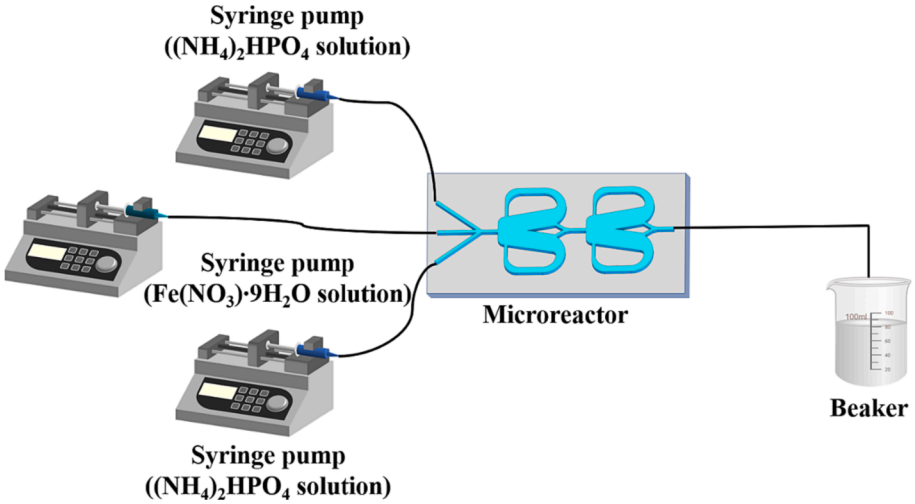

Fig. 5. Schematic of the continuous synthesis of $FePO_4$ NPs using the FOFM.

widely conducted to describe the overall mixing performance of a reactor, they could not provide detail local information on velocity and concentration fields. In addition, the mechanisms of mixing cannot be determined in detail through the experimental methods. Nonetheless, the CFD (computational fluid dynamics) simulation software is recognized as a powerful tool to analyze the local flow characteristic and to reveal the mixing mechanisms in the reactor.

3.1. Governing equations

The flow and concentration field inside a microreactor can be illustrated by the incompressible models including the following three governing equations for continuity, momentum, and species convection-diffusion.

$$\text{Continuityequation}: \nabla\cdot\vec{v} = 0 \tag{16}$$

$$\text{Momentum equation}: \rho\frac{\partial\vec{v}}{\partial t} + \rho\vec{v}\cdot\nabla\vec{v} = -\nabla P + \rho\vec{g} + \mu\nabla^2\vec{v} \tag{17}$$

$$\text{Speciesconvection}-\text{diffusionequation}: \frac{\partial C}{\partial t} + \vec{v}\cdot\nabla C = D\nabla^2 C + S \tag{18}$$

where $\vec{v}$, ρ, t, P, and μ is velocity vector, density, time, pressure, and dynamic viscosity, respectively, while C and D illustrates the concentration and diffusion coefficient of species, respectively. S represents the formation rate of species and is only considered when modelling the Villermaux–Dushman reaction.

3.2. Simulation procedures

For the simulation of fluid mixing, for the YOFM, dye water and water entered the reactor through the left and right passage of Y-junction inlet, respectively. With respect to the FOFM, blank water entered the reactor from the two sides of the focus entrance, while dye water from the middle passage. Since the concentration of the dye was extremely low, for simplicity, constant density (998.2 kg m^{-3}) and dynamic viscosity (1.003×10^{-3} kg m^{-1} s^{-1}) were utilized for the two feeds, and the dye diffusion coefficient D in the simulations was set as 2.2×10^{-9} m^2 s^{-1}. (Sun et al., 2007; Holz et al., 2000).

For the simulation of the Villermaux–Dushman reaction, the H_2SO_4 aqueous solution (0.03 mol/L) entered the reactor through the middle passage, while the buffer solution (0.0909 mol/L HBO_3^-, 0.0117 mol/L I^-, and 0.00233 mol/L IO_3^-) from the side inlets. Since liquid water in both acid solution and buffer solution accounts for more than 99% of the volume, for simplicity, constant density (998.2 kg m^{-3}) and dynamic viscosity (1.003×10^{-3} kg m^{-1} s^{-1}) were utilized for all species. (Chen et al., 2018) The diffusion coefficients of the species in water were shown in Table 1.

The finite volume method was adopted to discretize the above three governing equations, and the numerical simulations were conducted through the commercial software ANSYS Fluent 2021 operated in a double precision model. The three-dimensional (3D) geometry of the reactor was constructed by the Solidworks Solid Works 2016 software, then it was meshed into structured meshes with hexahedral elements by using the ICEM software. For the mesh-independent check, five different sizes of mesh with 3D cell number ranging from 324 060 to 2 213 706 were built for the FOFM, and a grid number of 1 609 410 (Fig. S3) was selected for CFD simulations based on calculation speed and accuracy. Similarly, a grid number of 1 560 306 was adopted for the YOFM. For the simulation of the Villermaux–Dushman reaction, the Finite Rate/No TCI was used to deal with the interaction between turbulence and reaction as the fluid flow was laminar in this study. The reaction rate constants were set as the same with those in the actual experiments (Table S1), except that the rate constant for the Dushman reaction (reaction (5) was simplified to 4.27×10^8 $L^4/(mol^4\cdot s)$. (Chen et al., 2022; Ouyang et al., 2017) To conform to the experimental conditions, suitable boundary conditions for CFD simulations were utilized: no-slip boundary condition for walls at constant temperature (25 °C), velocity inlet for inlets, and pressure outlet for outlets. Based on the results of flow rate investigation, an appropriate time step (1×10^{-6} – 1×10^{-4} s) was determined, and a residual error of 1×10^{-6} was adopted in all the cases to ensure solution accuracy.

Table 1
Diffusion coefficients of reactants (Leaist, 1984; Parkhurst and Appelo, 2013; Shi et al., 2012).

Species	Diffusion coefficient × 10^{-9} m^2 s^{-1}
H_2SO_4	2.420
H^+	9.311
HSO_4^-	1.330
SO_4^-	1.070
$H_2BO_3^-$	1.000
H_3BO_3	1.000
I^-	2.045
IO_3^-	1.078
I_2	1.360
I_3^-	1.000

4. Results and discussion

4.1. Flow pattern

As known, chaotic advection can continuously compress, stretch, split and break the fluid microclumps, which can effectively promote the surface renewal of fluid microclusters and reduce the mass transfer distance. Hence, it is important to induce secondary flows to generate chaotic advection. Because of the unique design of the inner structure of the OFM, there were three unique secondary flows in the FOFM, such as vortex, feedback, and oscillation, and the location as well as the size of vortex changed with time. The detail generation mechanism for the oscillating flow was described in the Supporting Information, while the evolution of the three unique secondary flows at Q_{total} = 8 mL/min in stage I of FOFM was described in Fig. 6.

At t = 0 s (Fig. 6a), the main vortex in the right mixing chamber was much larger than that in the left mixing chamber, and the oscillating flow swung to the left side, which induced much more fluid flowing into the left feedback channel than that flowing into the right feedback channel. When the time increased, the size of the left vortex increased with increasing the amount of the fluid in the left mixing chamber, and the vortex size in the left mixing chamber was a little larger than that in the right, resulting in the combined lateral force in the mixing chamber towards the right side, hence the inlet fluid gradually deflected to the right (Fig. 6b, t = 0.5 s). Similarly, as the time further increased, the amount of the fluid in the right mixing chamber would increase owing to the enhanced right feedback flow. The right vortex could be further developed and the size could be larger than that in the left, hence, the oscillating flow would swing back to the left side again because of the leftward lateral force (Fig. 6c, t = 1.0 s). Afterwards, with further increase of time to 1.5 s, the inlet fluid completely swung to the right side again with the size of left vortex obvious larger than that of right vortex (Fig. 6d, t = 1.5 s).

4.2. Mixing performance

Fig. 7 shows the change of flow pattern in YOFM and FOFM. At Q_{total} = 4 mL/min (Fig. 7a, 7b), the mixing in stage I of YOFM and FOFM was poor, and just some light blue fluids could be found in the right feedback channels. This is because the feedback flow cannot be effectively induced at low flow rates. It can be seen that the mixing in the stage II of YOFM shows no significant improvement compared to that in stage I, but more even mixing was observed in the stage II of FOFM in comparison to that in stage I. At Q_{total} = 6 mL/min (Fig. 7c and d), much

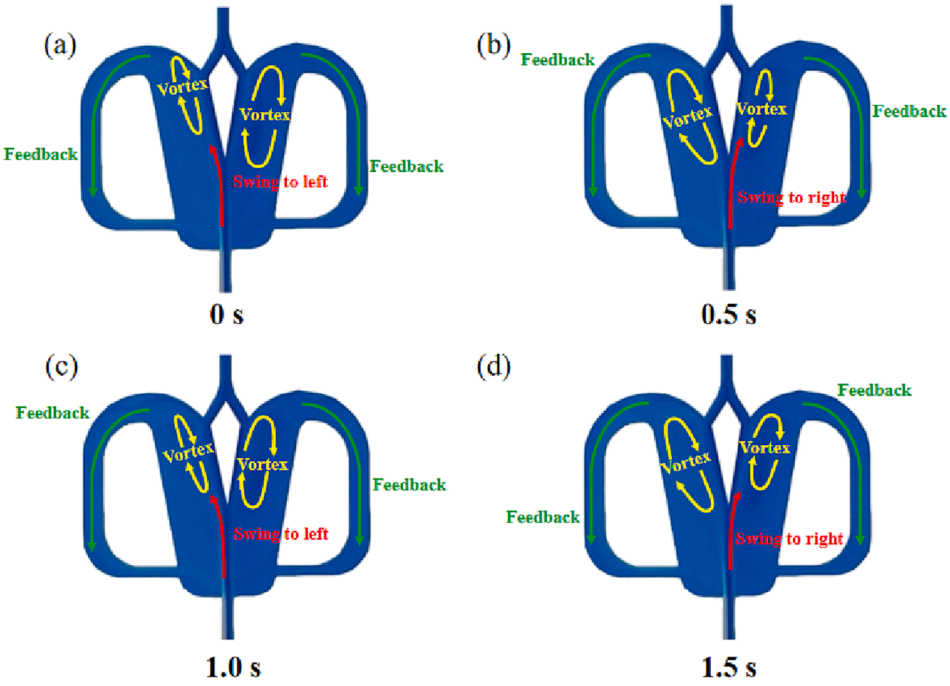

Fig. 6. Evolution of the three unique secondary flows at Q_{total} = 8 mL/min in stage I of FOFM.

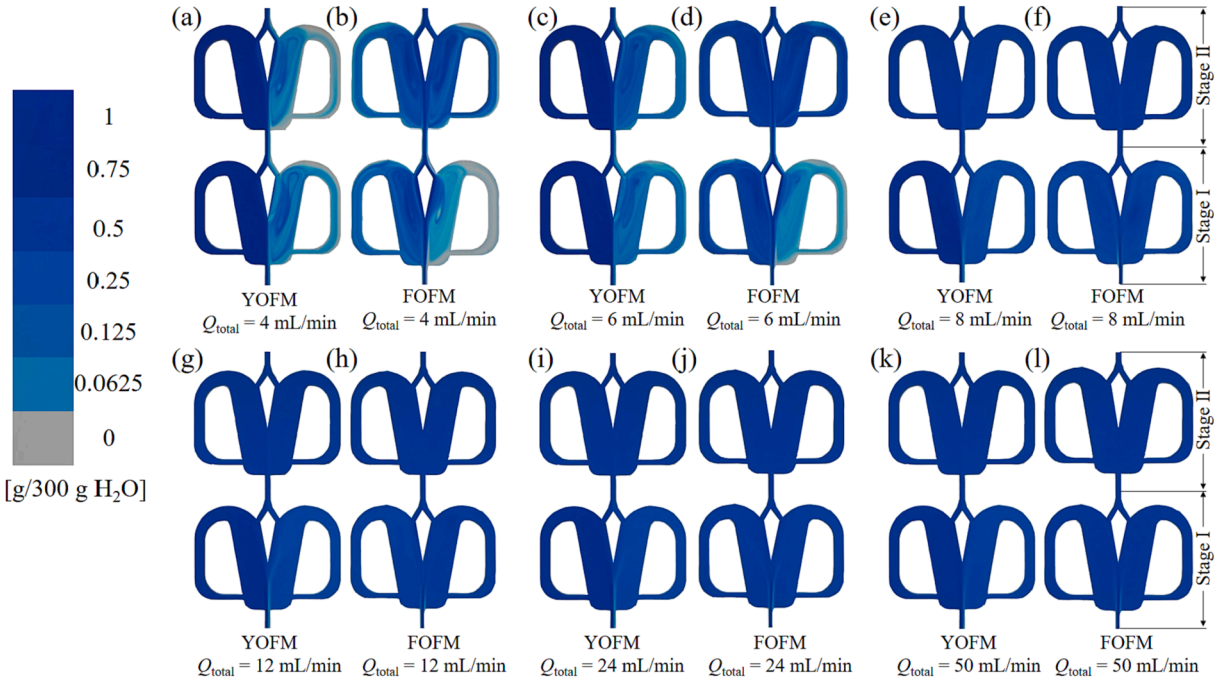

Fig. 7. The concentration field images for the fluid mixing process in YOFM (a,c,e,g,i,k) and FOFM (b,d,f,h,j,l) at different inlet flow rates; (a,b): 4 mL/min, (c,d): 6 mL/min, (e,f): 8 mL/min, (g,h): 12 mL/min, (i,j): 24 mL/min, (k,l): 50 mL/min.

better mixing was achieved in stage II of the two OFMs (Fig. 7a and b), and almost complete mixing was observed in stage II of FOFM, showing more uniform mixing in comparison to that of YOFM.

When $Q_{total} \geq 8$ mL/min (Fig. 7e – l), the mixing in stage I for the two OFMs significantly improved (Fig. 7c and d), and the *MI* of FOFM was a little larger than that of YOFM at equal flow rates (Fig. 8). This phenomenon can be explained as follows: with the increase of flow rate, the three unique secondary flows (vortex, feedback, and oscillation) can be effectively generated, which can remarkably enhance chaotic advection mixing. Hence, the mixing in stage I for both OFMs was significantly improved as the flow rate was increased from 6 to 8 mL/min. It was observed that above Q_{total} = 8 mL/min, the increase of flow rate has little effect on the mixing efficiency of YOFM and FOFM. However, it should be noted that the *MI* in stage II of FOFM was up to 100%, whereas that of YOFM was only 97.3% at Q_{total} = 50 mL/min (Fig. 8).

4.3. Mechanistic analysis of mixing enhancement in FOFM

From the above dye-tracer experiments, it is apparent that FOFM displayed better mixing performance than YOFM, but the reason is

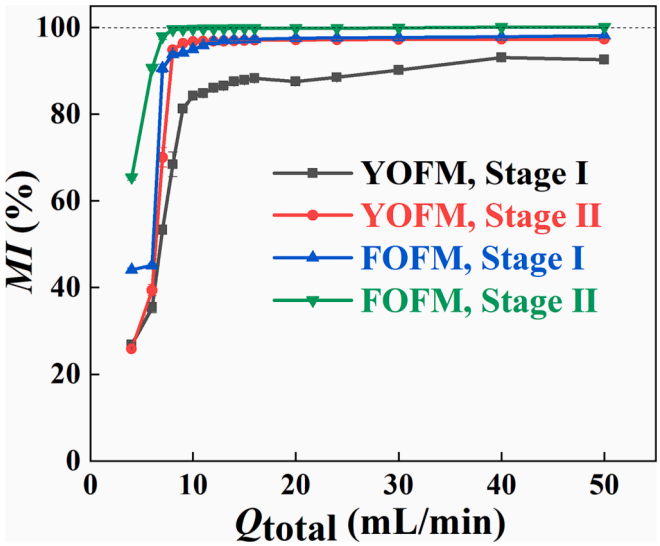

Fig. 8. Mixing index *MI* in YOFM and FOFM at different flow rates.

unclear. Herein, we used 3D CFD simulation to study the flow field and concentration field. Depicted in Fig. 9 is the concentration field at middle cross section of YOFM and FOFM. The simulation results suggest that at equal flow rates, the mixing performance in FOFM is better than that in YOFM, in good agreement with the results of dye-tracer experiments. Two main reasons may account for this phenomenon: (1) A more efficient chaotic advection mixing might be achieved in FOFM, namely, the three unique secondary flows (vortex, feedback, and oscillation) in FOFM were much stronger than those in YOFM; (2) The premixing in the flow-focused inlet channel of FOFM was much stronger than that in the Y-junction inlet of YOFM.

With respect to the first reason, here, we investigated the chaotic advection characteristics (vortex, feedback, and oscillation) in stage I for the two OFMs. For the vortex flow, we adopted velocity swirling strength (Fig. 10) and velocity vorticity magnitude (Fig. S6) as indicators to describe the vortex intensity. As shown in Fig. 10, at Q_{total} = 6 mL/min, the largest velocity swirling strength in YOFM (1589.6 s^{-1}) is larger than that in FOFM (1037.3 s^{-1}), indicating that the vortex flow induced in YOFM is more intense than that in FOFM. This phenomenon can be explained as follows: Because the blank water of FOFM is split into two equal parts by the flow-focused side inlets, the velocity of the non-split blank water of YOFM is larger than that in FOFM. In addition, at Q_{total} = 6 mL/min, due to insufficient momentum exchange in stage I of FOFM owing to the low flow rate, the vortex flow induced in YOFM is more intense than that in FOFM. At Q_{total} = 8 or 12 mL/min, however, there is no significant difference between FOFM and YOFM in velocity swirling strength, owing to the sufficient momentum exchange in stage I of both cases. Similar results were observed in the study of velocity vorticity magnitude as showed in Fig. S6.

For the feedback flow, we adopted mass flow rates (Fig. 11a and b, Fig. S7a and b) and static pressure (Fig. 11c and d, Fig. S7c and d) in the feedback channels as indicators to describe the intensity of feedback flow in the reactor. As showed in Fig. 11 and Fig. S7, in stage I at same flow rates, YOFM and FOFM are almost similar in mass flow rate (or static pressure) in the left/right feedback channel, indicating that the feedback flow strengths of the two OFMs are approximately equal. In addition, the effects of grid size (i.e., grid number) and the time interval (i.e., time step) on the simulation of the feedback flow were described in the Supporting Information (Fig. S8, and Fig. S9).

For the oscillating flow, we adopted oscillating frequency *f* in stage I as an indicator to describe the oscillating intensity. Noted that the oscillating frequency was obtained through the fast Fourier transform based on pressure signal in the left feedback channel (Fig. 11c and Fig. S7c). As showed in Fig. 12, the *f* of YOFM and FOFM at equal flow rates are largely the same. In addition, as illustrated in Fig. S11, both the frequencies increase with the increase of the inlet flow rates, and a similar linear relation between flow rate and oscillation frequency can be obtained as Q_{total} in the range of 6–14 mL/min, indicating that the two OFMs are approximately equal in oscillation flow strength.

Furthermore, YOFM and FOFM are almost similar in average strain rate (Fig. S12) in middle cross section (h = 0.5 mm) at different inlet flow rates, indicating that the chaotic flow strengths of the two OFMs are approximately equal.

With respect to the second reason, four monitoring planes (i.e., plane-0, plane-left, plane-right, and plane-1 showed in Fig. S13) were adopted to describe the effect of the two different inlet structures. As shown in Fig. 13, for the plane-0, much better mixing performance was achieved in FOFM than in YOFM at same flow rates. This is because there were two fluid contact surfaces in the flow-focused inlet, while just one in the Y-junction inlet, thus the mass transfer surface area for the flow-focused inlet was much larger than that for the Y-junction inlet. Noted that the flow rates presented no significant influence on the mixing performance in plane-0 for both inlet structures. This phenomenon can be explained as follows: The molecular diffusion based on molecular thermal motion is the main mass transfer mode to mix the two fluids in the inlet channel, which mainly relies on the temperature and concentration. Hence, the flow rates had no significant effect on the mixing performance of plane-0 in both inlets. On the contrary, the mixing efficiency of plane-1 (Fig. 13d–f, j–l), plane-left (Fig. S14) and plane-right (Fig. S15) significantly increased with the increase of flow rates, and presented much better mixing performance than that in plane-0 at same flow rates. This is because the chaotic advection mixing is the main mass transfer mode in the mixing chamber, and the chaotic intensity increases with the increase of the flow rates. Furthermore, the mixing efficiency of plane-1 (Fig. 13d–f, j–l), plane-left (Fig. S14) and plane-right (Fig. S15) in FOFM was much higher than those in YOFM at same flow rates, indicating that the premixing in the inlets was pivotal for promoting fluid mixing in stage I of the OFMs.

In summary, the change of the inlet structure would not change the chaotic mixing characteristics of OFMs, while the efficient premixing in the inlets is the key for enhancing overall fluid mixing. These are valuable guidelines for the design and structure optimization of OFMs.

4.4. Microscale mixing

According to the results of dye-tracer experiments and CFD simulations, it is disclosed that the mixing performance of FOFM is better than that of YOFM. Hence, FOFM was selected for high-throughput production of $FePO_4$ NPs, where a preknowledge of micormixing process at molecular scale is helpful for controlled synthesis of the NPs. In this section, the micromixing performance of FOFM was studied by Villermaux-Dushman experiments and CFD simulations to investigate the influence of flow rates, flux ratio *R*, and H^+ ions concentration on micromixing.

4.4.1. Effect of flow rates

To investigate the effect of flow rate on microscale mixing in FOFM, a buffer solution (0.1818 mol/L H_3BO_3, 0.0909 mol/L NaOH, 0.0117 mol/L KI, and 0.00233 mol/L KIO_3) was prepared and pumped into the reactor from the side inlets, while an acid solution (0.03 mol/L H_2SO_4) was pumped in from the middle inlet.

Fig. 14a and d shows the changes of separation index X_S and micromixing time τ_m versus flow rates in FOFM, respectively. The results show that when Q_{total} <20 mL/min, there was significant decrease of X_S and τ_m with the increase of inlet flow rates, indicating that the micromixing process was effectively enhanced with increasing flow rate. When Q_{total} was increased from 20 to 50 mL/min, the decrease of X_S and τ_m became much less significant. It should be noted that the shortest microscale mixing time τ_m was 0.16 ms, indicating that a fast and

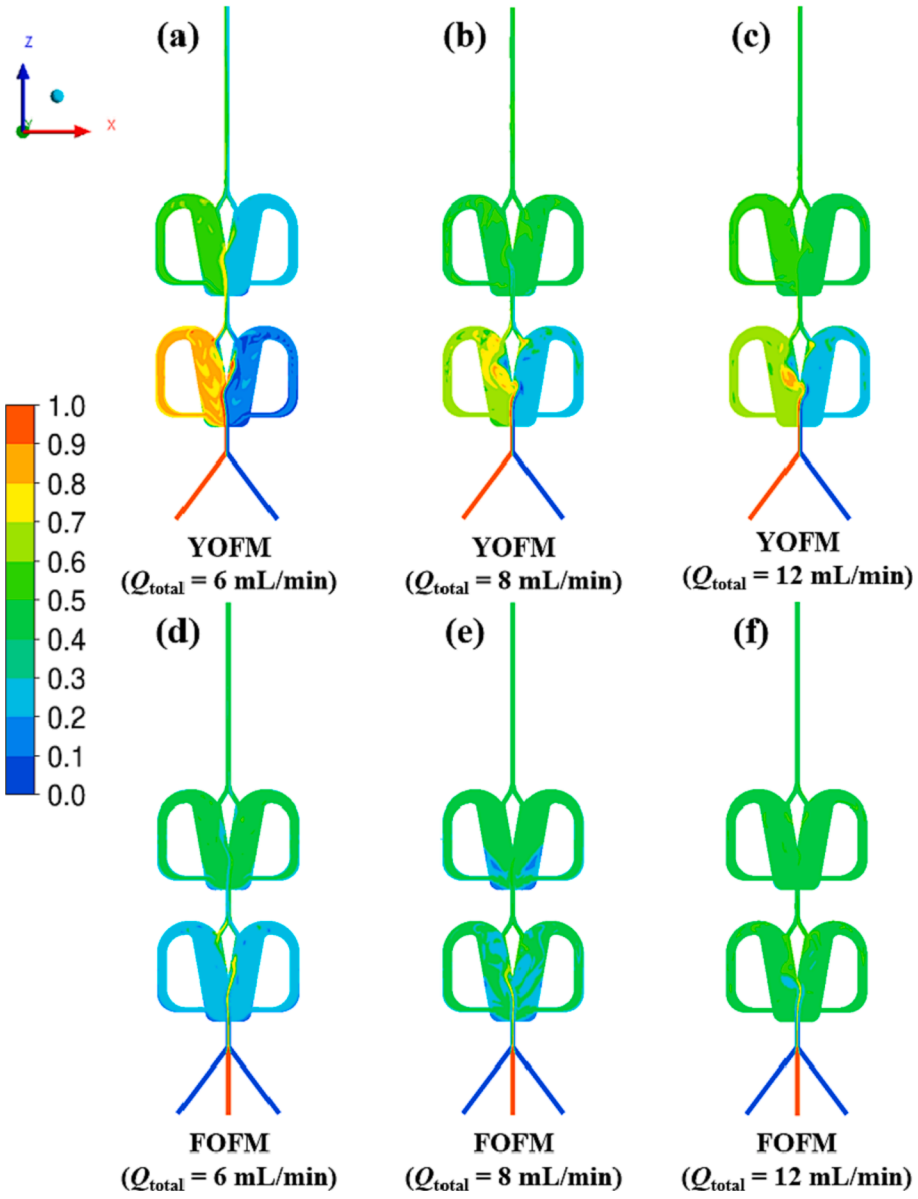

Fig. 9. Concentration in middle cross section (h = 0.5 mm) of (a,b,c) YOFM and (d,e,f) FOFM at different inlet flow rates; (a,d): 6 mL/min, (b,e): 8 mL/min, (c,f): 12 mL/min.

efficient micromixing process could be established in the FOFM. It is hence envisioned that uniform concentration and temperature fields can be provided for the nucleation and growth of $FePO_4$ NPs.

4.4.2. *Effect of flux ratio*

In the investigation of the effect of flux ratio on the microscale mixing of FOFM, it was noted that with the variation of flux ratio, the following equations have to be satisfied to keep the molar ratio of different ions constant. (Yang et al., 2021)

$$\frac{3V_1\left[IO_3^-\right]_0}{V_2[H^+]_0} = C_1 \tag{19}$$

$$\frac{V_1\left[H_2BO_3^-\right]_0}{V_2[H^+]_0} = C_2 \tag{20}$$

where C_1 and C_2 are constants. The concentrations of different reactants adopted in the study are described in Table S3. To avoid natural generation of I_2 in the absence of acid aggregates, the concentrations for different reactants must be carefully selected to maintain a system pH of 8.5. (Yang et al., 2021) The total flow rate was kept constant at Q_{total} = 12 mL/min in all the experiments.

Fig. 14b and e shows the changes of X_S and τ_m versus R, respectively. With R increased from 1 to 3, X_S increased from 0.0018 to 0.0156. This phenomenon can be explained as follows: On one hand, with the increase of R, there is improvement of mixing performance, and thus the decrease of X_S and τ_m. On the other hand, according to Eqs. (19) and (20), with the increase of R, there is increase of H^+ ions concentration. The local Dushman reaction rate (Eq. (5)) determined by the local concentrations of the reactants would increase with increasing concentration of H^+ ions, hence the increase of X_S and τ_m (Fig. 14c and f). In summary, the X_S is jointly determined by the mixing performance and H^+ ions concentration, thus X_S may increased and τ_m decreased with the increase of R (Fig. 14b and e).

4.4.3. *Effect of H^+ ions concentration*

To investigate the effect of H^+ ions concentration on the microscale mixing process of FOFM, buffer solution (i.e., 0.1818 mol/L H_3BO_3, 0.0909 mol/L NaOH, 0.0117 mol/L KI, and 0.00233 mol/L KIO_3) was

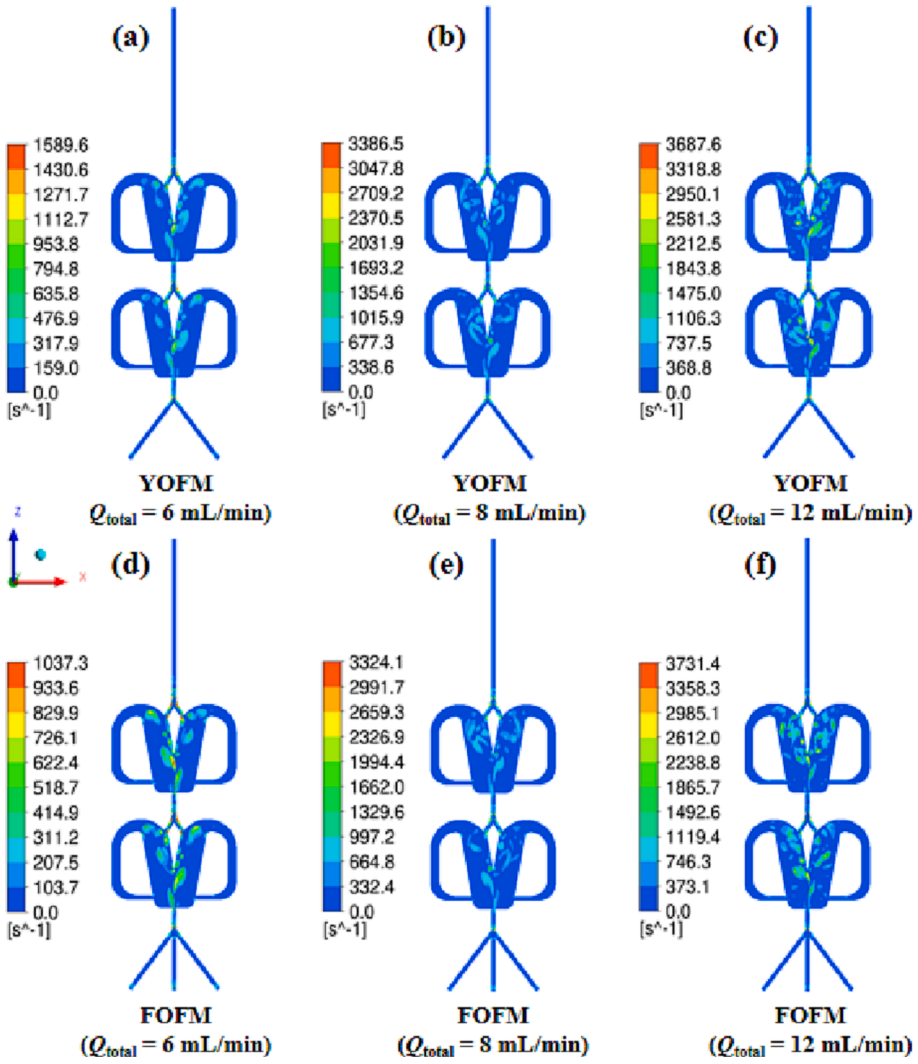

Fig. 10. Velocity swirling strength in middle cross section (h = 0. 5 mm) of (a,b,c) YOFM and (d,e,f) FOFM at different inlet flow rates; (a,d): 6 mL/min, (b,e): 8 mL/min, (c,f): 12 mL/min.

pumped into the reactor from the side inlets, while the acid solution of a certain concentration was pumped in from the middle inlet. The total flow rates were varied from 8 to 20 mL/min.

As revealed in Fig. 14c and f, when Q_{total} ≥12 mL/min, there is no significant change of X_S (Fig. 14c) and τ_m (Fig. 14f) with increasing H^+ ions concentration. When Q_{total} <12 mL/min, however, the X_S and τ_m increased with the increase of H^+ ions concentration. This phenomenon can be explained as follows: When Q_{total} ≥12 mL/min, the chaotic advection is intense, and hence fast and uniform mixing is achieved under the condition of high H^+ ions concentration. Consequently, the H^+ ions concentration has no significant effect on X_S and τ_m as Q_{total} ≥12 mL/min.

4.4.4. CFD simulations

In order to obtain the local concentration distribution of the species for the Villermaux–Dushman reaction in FOFM, direct CFD simulations were conducted. Fig. 15a–d shows the molar concentration contours of H^+, $H_2BO_3^-$, H_3BO_3, and I_2 in the cross section of FOFM, respectively.

Since reaction (4) occurs rather quickly, the majority of H^+ was rapidly consumed in the diverging mixing chamber of the first stage to produce H_3BO_3 (Fig. 15a–c). As shown in Fig. 15d, a small amount of I_2 could be found in stage I owing to local excess H^+. Combined with Fig. 14a, it can be seen that the micromixing process can be further enhanced by increasing the flow rates, inhibiting the production of I_2 due to a more uniform concentration distribution of H^+. In addition, the *Xs* calculated by CFD simulation at different flow rates was shown in Fig. S16, which indicated that *Xs* decreased with increasing inlet flow rates, presenting similar trend with the experimental results. However, the simulation results of *Xs* were obviously less than those of experimental results, which is because the precise micromixing model involving species mixing was not adopted owing to the limited computational resource, and similar discussions can also be found in other literature (Ouyang et al., 2017).

4.5. Characterization of iron phosphate nanoparticles

Fig. S17 depicts the XRD patterns of the samples prepared in FOFM, while Fig. S18 displays those of the sample prepared by batch method. All of them are consistent with that of $FePO_4$ in standard JCPDS card (No. 29–0715), indicating that pure $FePO_4$ NPs were successfully prepared.

4.6. Effect of flow rates on preparing iron phosphate

Fig. 16 shows the SEM images of $FePO_4$ NPs prepared using FOFM at different flow rates. The initial concentrations of the two reactants (C_0) are both 0.1 mol/L. The results indicate that with the increase of total flow rate (Q_{total}: from 20 to 180 mL/min), the average particle size of the

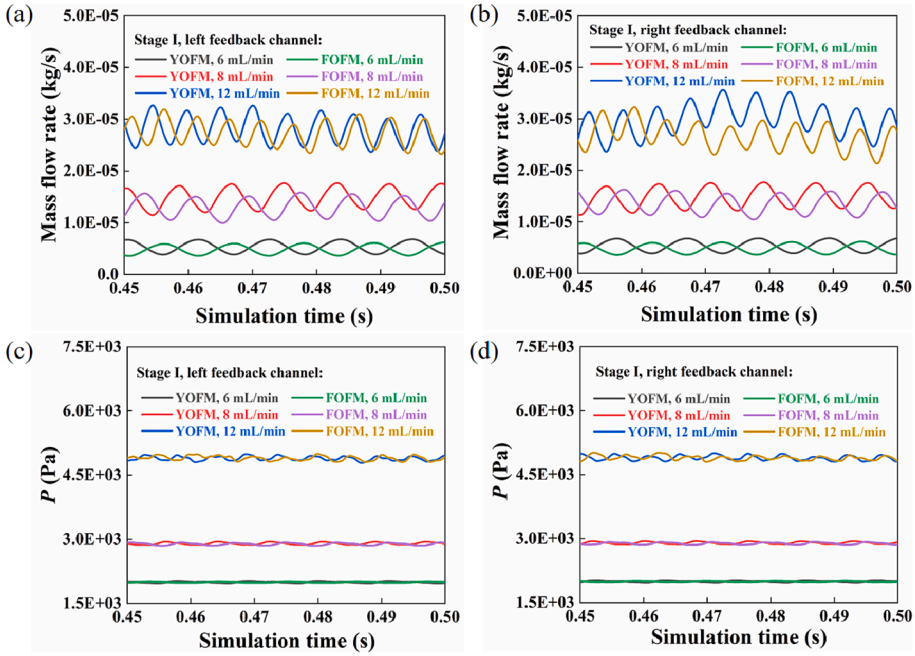

Fig. 11. (a,b) Mass flow rates and (c,d) static pressure in the (a,c) left and (b,d) right feedback channels in stage I of YOFM and FOFM at different inlet flow rates.

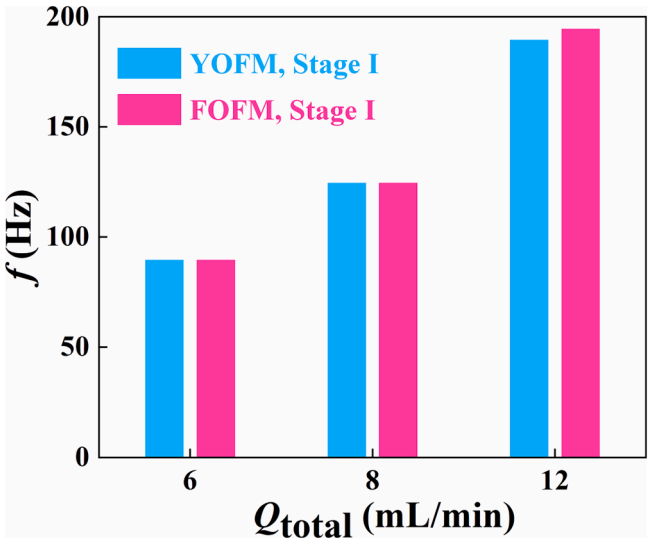

Fig. 12. Oscillating frequency in stage I of YOFM and FOFM at different inlet flow rates.

samples decreased (d: from 22 to 17 nm) and the PSD became narrower (σ_g: from 1.14 to 1.09 nm). This phenomenon can be explained as follows: according to the results of dye tracer and Villermaux–Dushman experiments, with the increase of flow rates, more efficient mixing can be achieved in FOFM, which results in more uniform concentration and temperature fields in a shorter time, leading to more consumption of precursors for nucleation rather than for the growth of $FePO_4$ nanocrystals. Hence, small $FePO_4$ nanocrystals with narrower PSD could be produced with the increase of flow rate. It should be noted that a similar phenomenon has also been found in other similar chaotic microreactors, (Liu et al., 2022a; Wei et al., 2022) thus one common rule can be concluded: Because the average size and PSD of the nanocrystals are closely related to the uniformity and magnitude of supersaturation for the reaction systems. Due to the high mixing efficiency for the OFMs, one can easily adjust the average size and PSD of the nanoparticles by simply changing the flow rates (i.e., the supersaturation). Furthermore, noted that the largest throughput was 180 mL/min, which was much larger than those possible in conventional lamination (Hakke et al., 2021) and segment flow (Hao et al., 2019) microreactors.

In addition, it should be noted that there was no clogging of channel during the preparation of $FePO_4$ NPs using FOFM. This can be explained as follows: (1) After each experiment, the reactor was immediately and repeatedly washed at least three times using deionized water to remove residual reactants and prevent clogging; (2) Uniform concentration filed for nucleation and growth of NPs can be achieved owing to the high-efficient chaotic advection mixing in the FOFM, which can effectively prevent the formation of large particles that may block channels; (3) The fluid can be effectively stretched, folded, squeezed and broken-up at high throughput (10–180 mL/min), which can effectively prevent particles from agglomeration, as well as attaching and adhering to the channel walls due to strong fluid shear force.

4.7. *Effect of reactant concentration on preparing iron phosphate*

Fig. 17 illustrates the SEM images of $FePO_4$ NPs prepared by FOFM at different initial reactant concentrations. The total flow rate was kept as 180 mL/min, and the pH for the $FePO_4$ preparation was presented in Table S2. It was found that the average size of the prepared samples decreased with the increase of the reactant concentrations. This phenomenon can be explained as follows: With the increase of reactant concentrations, there is increase of supersaturation, and more precursors would be used for crystal nucleation rather than for crystal growth, thus the size decrease of the samples. It should be noted that ultra-small $FePO_4$ NPs (d = 9 nm) with narrow PSD (σ_g = 1.13) was produced at an initial reactant concentration of 0.9 mol/L, and in other microreactors the particle size would be larger. (Lu et al., 2012; Zhang et al., 2013).

It should be noted that the P/Fe molar ratio is another important index to evaluate the quality of $FePO_4$ particles in industry. ICP-AES was used to determine the P/Fe molar ratio of the prepared samples. The results of P/Fe molar ratio of the samples obtained at different reactant concentrations are shown in Table 2. The results indicate that the P/Fe molar ratios of the products synthesized at different reactant concentrations were close to the expected stoichiometric ratio of 1, confirming

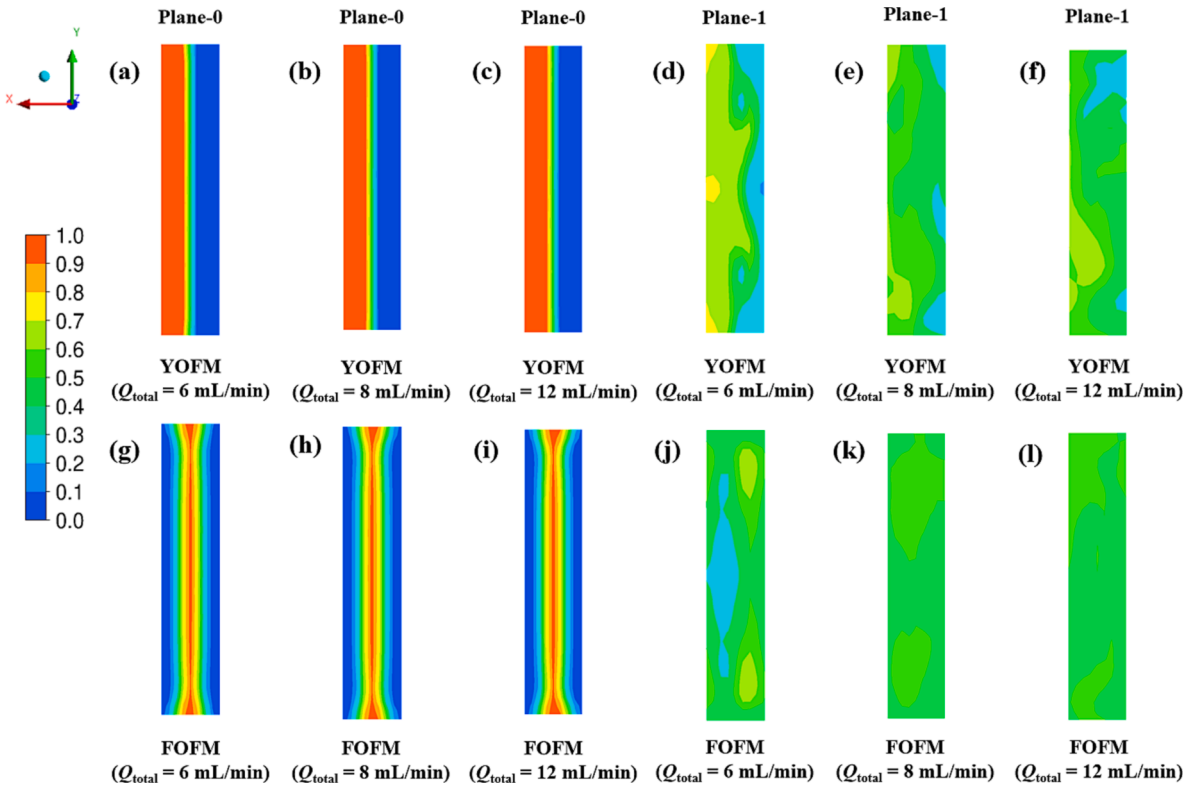

Fig. 13. Concentration in different longitudinal sections (plane-0: a–c, g–i; plane-1: d–f, j–l) of (a–f) YOFM and (g–l) FOFM at different inlet flow rates; (a,d,g,j): 6 mL/min, (b,e,h,k): 8 mL/min, (c,f,i,l): 12 mL/min.

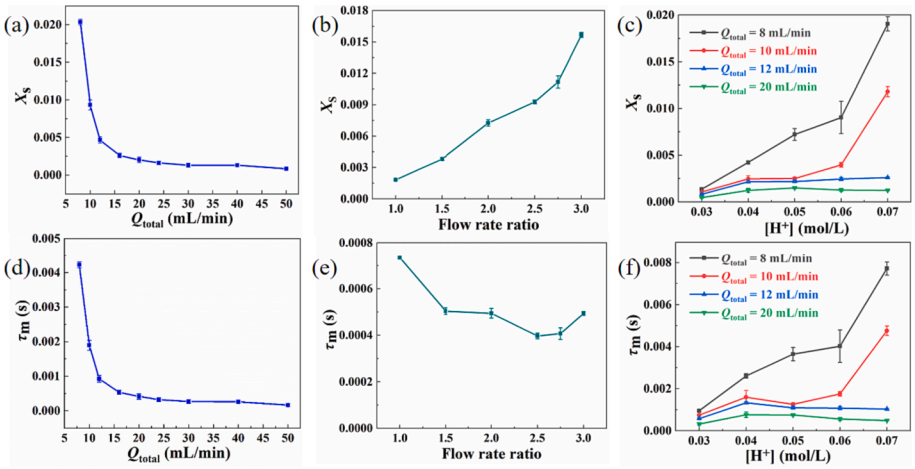

Fig. 14. Separation index X_S and micromixing time τ_m at different (a, d) inlet flow rates when $R = 1$, (b, e) flux ratios when $Q_{total} = 12$ mL/min, and (c, f) H^+ ions concentrations when $R = 1$.

that the microreactor method could guarantee the purity of $FePO_4$ NPs.

4.8. Comparison with batch method

Fig. S19 illustrates the SEM and PSD images of $FePO_4$ NPs prepared by batch method at a reactant concentration of 0.1 mol/L. It can be found that the batch method produced $FePO_4$ NPs with size ($d = 26$ nm) and PSD ($\sigma_g = 1.14$) larger than those prepared by the microreactor method (Fig. 16, d = 17–21 nm, σ_g = 1.09–1.14). This is because the poor mixing of batch mode results in uneven concentration and temperature fields for the nucleation and growth of $FePO_4$ NPs. Noted that this phenomenon would intensify when the batch process is subject to scale up production.

5. Conclusions

In this study, two kinds of high-throughput oscillating feedback microreactors (OFMs) were designed based on chaotic advection. Through dye-tracer experiments and CFD simulations, it is concluded that the flow-focused OFM (FOFM) presented better mixing performance than the Y-junction OFM (YOFM), owing to the more efficient premixing ability of the FOFM inlet channels. The results of Villermaux-Dushman experiments indicated that almost complete mixing could be achieved in 0.16 ms at a total flow rate of 50 mL/min. Overall, high-purity (P/Fe molar ratio: 0.95–1.04) and ultra-small (9 nm) iron phosphate nanoparticles with narrow particle size distribution could be produced at a high throughput of 180 mL/min using FOFM, and the size

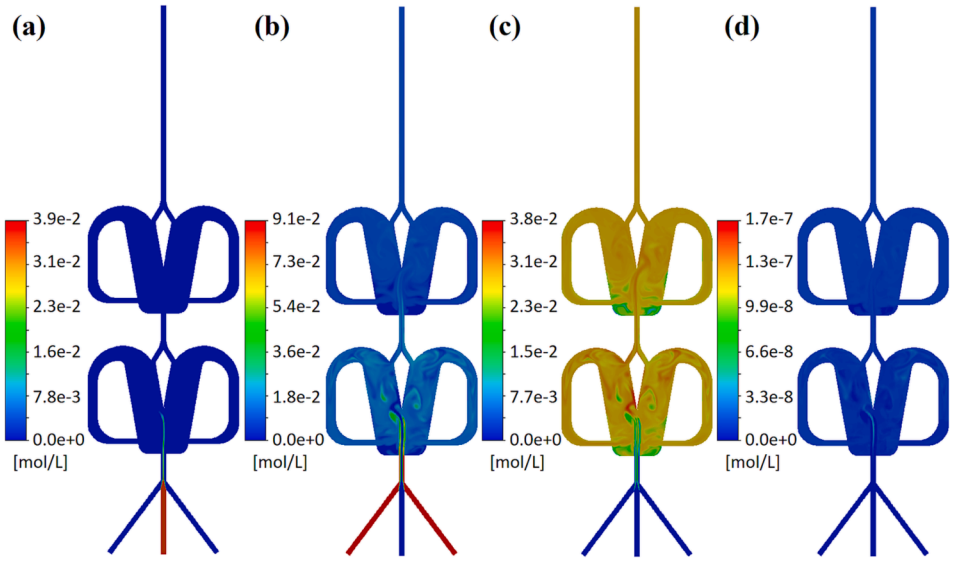

Fig. 15. Molar concentration contours in middle cross section of FOFM at Q_{total} = 12 mL/min, (a) H^+, (b) $H_2BO_3^-$, (c) H_3BO_3, (d) I_2. (R = 1, = 0.03 mol/L).

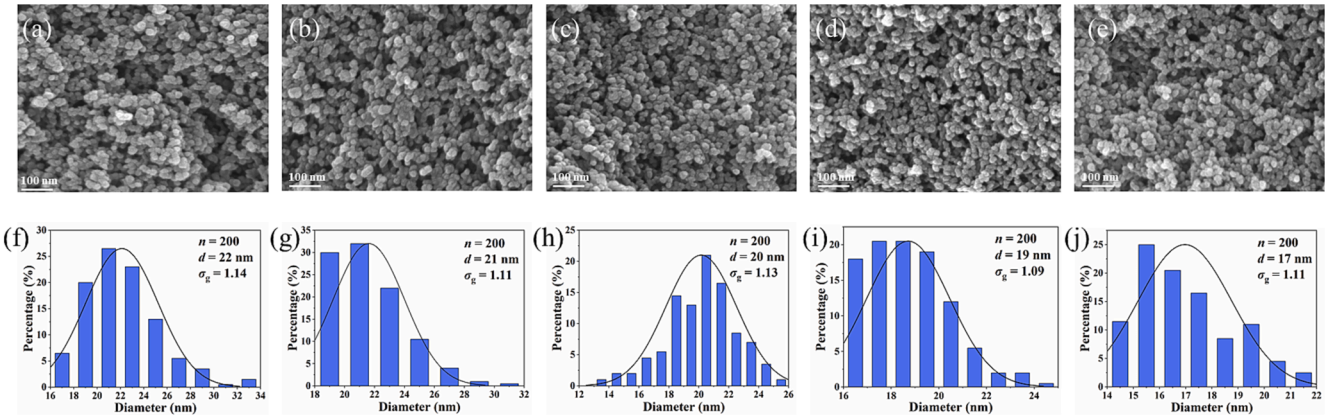

Fig. 16. (a–e) SEM images and (f–j) particle size distribution of $FePO_4$ NPs synthesized at different total flow rates in FOFM; (a,f): Q_{total} = 10 mL/min, (b,g): Q_{total} = 20 mL/min, (c,h): Q_{total} = 60 mL/min, (d,i): Q_{total} = 120 mL/min, (e,j): Q_{total} = 180 mL/min; C_0 = 0.1 mol/L.

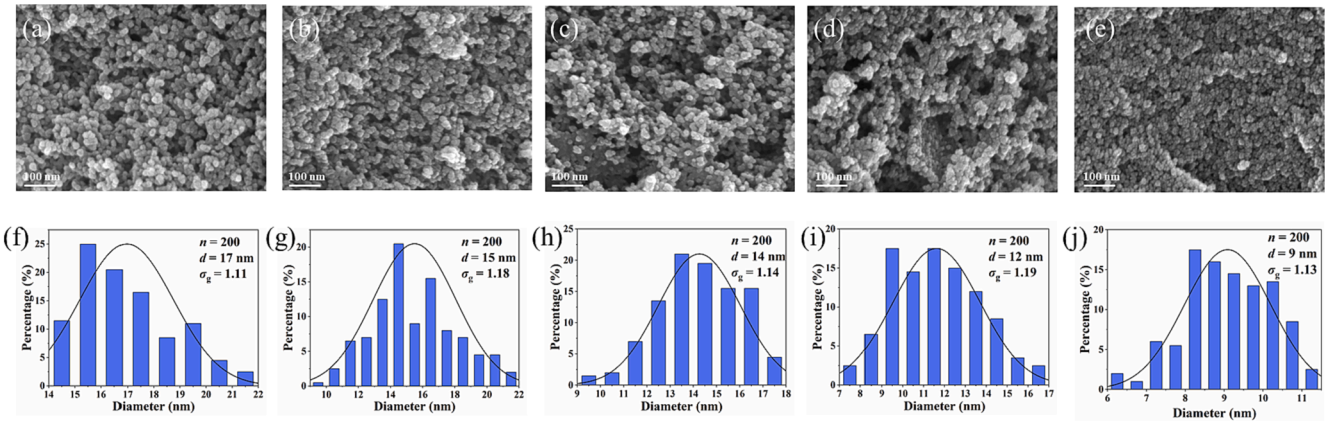

Fig. 17. (a–e) SEM and (f–j) particle size distribution images of iron phosphate NPs synthesized at different initial reactant concentrations (C_0) in FOFM; (a,f): C_0 = 0.1 mol/L, (b,g): C_0 = 0.3 mol/L, (c,h): C_0 = 0.5 mol/L, (d,i): C_0 = 0.7 mol/L, (e,j): C_0 = 0.9 mol/L; Q_{total} = 180 mL/min.

of $FePO_4$ NPs can be adjusted by simply changing the flow rate and/or initial concentration of the reactants. It is envisaged that the designed microreactor has potential applications in the synthesis of nanoparticles of other kind.

Declaration of Competing Interest

The authors declare that they have no known competing financial interests or personal relationships that could have appeared to influence

Table 2
P/Fe molar ratio of iron phosphate NPs prepared at different precursor concentrations.

Precursor concentration, mol/L	P, wt %	Fe, wt %	P/Fe, molar ratio
$C_0 = 0.1$	15.5	26.8	1.04
$C_0 = 0.5$	15.1	27.9	0.97
$C_0 = 0.9$	14.9	28.2	0.95

the work reported in this paper.

Data availability

Data will be made available on request.

Acknowledgements

This project was financially supported by the National Natural Science Foundation of China [Grants 22108066, 21725602 and 21938002]; the Natural Science Foundation of Hunan Province [Grant 2021JJ40048]; the Innovative Research Groups of Hunan Province [Grant 2019JJ10001]; and the Science and Technology Planning Project of Hunan Province [Grant 2019RS3010].

Appendix A. Supplementary data

Supplementary data to this article can be found online at https://doi.org/10.1016/j.ces.2023.119084.

References

Arian, E., Pauer, W., 2021a. A comprehensive investigation of the incorporation model for micromixing time calculation. Chem. Eng. Res. Des. 175, 296–308. https://doi.org/10.1016/j.cherd.2021.09.010.

Arian, E., Pauer, W., 2021b. Contributions to the kinetics of the iodide–iodate test reaction for micromixing time calculation with extended incorporation models. Chem. Eng. Sci. 237, 116549 https://doi.org/10.1016/j.ces.2021.116549.

Arian, E., Pauer, W., 2022. Progress in buffer choice for the Villermaux-Dushman reaction. Ind. Eng. Chem. Res. 61 (26), 9192–9205. https://doi.org/10.1021/acs.iecr.2c00825.

Asano, S., Maki, T., Inoue, S., Sogo, S., Furuta, M., Watanabe, S., Muranaka, Y., Kudo, S., Hayashi, J., Mae, K., 2023. Incorporative mixing in microreactors: Influence on reactions and importance of inlet designation. Chem. Eng. J. 451, 138942 https://doi.org/10.1016/j.cej.2022.138942.

Baqueiro, C., Ibaseta, N., Guichardon, P., Falk, L., 2018. Influence of reagents choice (buffer, acid and inert salt) on triiodide production in the Villermaux-Dushman method applied to a stirred vessel. Chem. Eng. Res. Des. 136, 25–31. https://doi.org/10.1016/j.cherd.2018.04.017.

Cao, Z.H., Ma, B.Z., Wang, C.Y., Shi, B.D., Chen, Y.Q., 2022. Thermodynamic analysis and application for preparing $FePO_4$ from nitric acid pressure leach laterite residue by selective leaching in phosphoric acid and induced precipitation. Hydrometallurgy 212, 105896. https://doi.org/10.1016/j.hydromet.2022.105896.

Chen, K.P., Liu, C.Y., Guo, T.Y., Wen, L.X., 2018. CFD and experimental investigations on the micromixing performance of single countercurrent-flow microchannel reactor. Chin. J. Chem. Eng. 27, 1079–1088. https://doi.org/10.1016/j.cjche.2018.11.026.

Chen, Q.C., Wang, L.B., Wang, K., Deng, J., Luo, G.C., 2022. Experimental and numerical investigation on the scaling-up of microsieve dispersion mixers. Ind. Eng. Chem. Res. 61 (36), 13383–13396. https://doi.org/10.1021/acs.iecr.2c02190.

Cui, C., Yang, C., Eidson, N., Chen, J.I., Han, F., Chen, L., Luo, C., Wang, P.F., Fan, X., Wang, C., 2020. A highly reversible, dendrite-free lithium metal anode enabled by a lithium-fluoride-enriched interphase. Adv. Mater. 32 (12), 1906427. https://doi.org/10.1002/adma.201906427.

Fan, W.T., Zhao, F., Dou, J.H., Guo, X.H., 2021. Continuous preparation of dual-mode luminescent $LaPO_4$: Tb^{3+}, Yb^{3+} nanoparticles by reactive flash nanoprecipitation. Chem. Eng. Sci. 242, 116734 https://doi.org/10.1016/j.ces.2021.116734.

Gaddem, M.R., Ookawara, S., Nigam, K.D.P., Yoshikawa, S., Matsumoto, H., 2022. Hydrodynamics and mixing in a novel design of compact microreactors: Arc flow inverters. Chem. Eng. Process. 180, 108770 https://doi.org/10.1016/j.cep.2021.108770.

Guichardon, P., Baqueiro, C., Ibaseta, N., 2021. Villermaux-Dushman test of micromixing characterization revisited: kinetic effects of acid choice and ionic strength. Ind. Eng. Chem. Res. 60, 18268–18282. https://doi.org/10.1021/acs.iecr.1c03208.

Hakke, V., Sonawane, S., Anandan, S., Sonawane, S., Ashokkumar, M., 2021. Process intensification approach using microreactors for synthesizing nanomaterials—A critical review. Nanomaterials 11, 98. https://doi.org/10.3390/nano11010098.

Hao, N., Xu, Z., Nie, Y., Jin, C., Closson, A.B., Zhang, M., Zhang, J.X.J., 2019. Microfluidics-enabled rational design of ZnO micro-/nanoparticles with enhanced photocatalysis, cytotoxicity, and piezoelectric properties. Chem. Eng. J. 378, 122222 https://doi.org/10.1016/j.cej.2019.122222.

Holz, M., Heil, S.R., Sacco, A., 2000. Temperature-dependent self-diffusion coefficients of water and six selected molecular liquids for calibration in accurate ^{1}H NMR PFG measurements. Phys. Chem. Chem. Phys. 2, 4740–4742. https://doi.org/10.1039/B005319H.

Kong, L., Chen, R., Wang, X., Zhao, C.-X., Chen, Q., Hai, M., Chen, D., Yang, Z., Weitz, D. A., 2019. Controlled co-precipitation of biocompatible colorant-loaded nanoparticles by microfluidics for natural color drinks. Lab Chip 19 (12), 2089–2095.

Kumar, J., Neiber, R.R., Park, J., Soomro, R.A., Greene, G.W., Mazari, S.A., Seo, H.Y., Lee, J.H., Shon, M., Chang, D.W., Cho, K.Y., 2022. Recent progress in sustainable recycling of $LiFePO_4$-type lithium-ion batteries: Strategies for highly selective lithium recovery. Chem. Eng. J. 431, 133993 https://doi.org/10.1016/j.cej.2021.133993.

Leaist, D.G., 1984. Diffusion in aqueous solutions of sulfuric acid. Can. J. Chem. 62 (9), 1692–1697.

Liu, Q., Wei, S.X., Shi, Z.C., Chen, H., Yang, H., Au, C.T., C.T., Xie, T.L., Yin, S.F.,, 2022a. High-throughput synthesis of uniform $Mg(OH)_2$ nanoparticles in an Oscillating Feedback Minireactor designed by the selective dimension scale-out method. Ind. Eng. Chem. Res. 61, 15820–15831. https://doi.org/10.1021/acs.iecr.2c01965.

Liu, Y., Yang, G.Z., Hui, Y., Ranaweera, S., Zhao, C.X., 2022b. Microfluidic nanoparticles for drug delivery. Small 18, 2106580. https://doi.org/10.1002/smll.202106580.

Lu, Y.C., Zhang, T.B., Liu, Y., Luo, G.S., 2012. Preparation of $FePO_4$ nano-particles by coupling fast precipitation in membrane dispersion microcontactor and hydrothermal treatment. Chem. Eng. J 210, 18–25. https://doi.org/10.1016/j.cej.2012.08.077.

Meng, E.C., Sun, J.L., Huang, Y., Tang, H.J., 2022. Morphology evolution and improved electrochemical properties of $LiFePO_4$ cathode materials for Li-ion batteries. Int. J. Electrochem. Sci. 17, 221225 https://doi.org/10.20964/2022.12.25.

Ouyang, Y., Xiang, Y., Zou, H.K., Chu, G.W., Chen, J.F., 2017. Flow characteristics and micromixing modeling in a microporous tube-in-tube microchannel reactor by CFD. Chem. Eng. J. 321, 533–545. https://doi.org/10.1016/j.cej.2017.03.151.

Park, K., Gil, B., Yun, A.J., Cho, J., Kim, J., Park, B., 2022. Mixed-Valence iron phosphate as an effective catalytic host for the high-rate lithium-sulfur battery. Chem. Eng. J. 435, 134814 https://doi.org/10.1016/j.cej.2022.134814.

Parkhurst, D.L., Appelo, C.A.J., 2013. Description of input and examples for PHREEQC Version 3—A computer program for speciation, batch-reaction, one-dimensional transport, and inverse geochemical calculations. U.S. Geological Survey Techniques and Methods, book 6, chap. A43, 497 p. https://pubs.usgs.gov/tm/06/a43/.

Pekkari, A., Say, Z., Susarrey-Arce, A., Langhammer, C., Härelind, H., Sebastian, V., Moth-Poulsen, K., 2019. Continuous microfluidic synthesis of Pd nanocubes and PdPt core–shell nanoparticles and their catalysis of NO_2 reduction. ACS Appl. Mater. Interfaces 11 (39), 36196–36204.

Shi, X., Xiang, Y., Wen, L.X., Chen, J.F., 2012. CFD analysis of flow patterns and micromixing efficiency in a Y-Type microchannel reactor. Ind. Eng. Chem. Res. 51 (43), 13944–13952. https://doi.org/10.1021/ie300985q.

Stolzenburg, P., Lorenz, T., Dietzel, A., Garnweitner, G., 2018. Microfluidic synthesis of metal oxide nanoparticles via the nonaqueous method. Chem. Eng. Sci. 191, 500–510. https://doi.org/10.1016/j.ces.2018.07.007.

Sui, J.S., Yan, J.Y., Wang, K., Luo, G.S., 2020. Efficient synthesis of lithium rare-earth tetrafluoride nanocrystals via a continuous flow method. Nano Res. 13 (10), 2837–2846. https://doi.org/10.1007/s12274-020-2938-y.

Sun, Y.L., Sun, M.H., Cheng, W.D., Ma, C.X., Liu, F., 2007. The examination of water potentials by simulating viscosity. Comp. Mater. Sci. 38, 737–740. https://doi.org/10.1016/j.commatsci.2006.05.007.

Wei, S.X., Yang, H., Au, C.T., Xie, T.L., Yin, S.F., 2022. Mixing characteristic and high-throughput synthesis of cadmium sulfide nanoparticles with cubic hexagonal phase junctions in a chaotic millireactor. Langmuir 38, 14439–14450. https://doi.org/10.1021/acs.langmuir.2c02087.

Xie, X., Yang, Y., Zhou, H., Li, M., Zhu, Z., 2018. Quality monitoring methods of initial and terminal manufacture of $LiFePO_4$ based lithium ion batteries by capillary electrophoresis. Talanta 179, 822–827. https://doi.org/10.1016/j.talanta.2017.12.004.

Xu, C., Chu, Y.F., 2015. Experimental study on oscillating feedback micromixer for miscible liquids using the Coanda Effect. AIChE J. 61, 1054–1063. https://doi.org/10.1002/aic.14702.

Yang, M., Luo, L.M., Chen, G.W., 2020. Microfluidic synthesis of ultrasmall Co nanoparticles over reduced graphene oxide and their catalytic properties. AIChE J. 66, e16950.

Yang, H., Wei, S.X., Chen, H., Chen, L., Au, C.T., Xie, T.L., Yin, S.F., 2022. A high-throughput chaotic advection microreactor for preparation of uniform and aggregated barium sulfate nanoparticles. AIChE J. 68 (10), e17810.

Yang, M., Yang, L., Zheng, J., Hondow, N., Bourne, R.A., Bailey, T., Irons, G., Sutherland, E., Lavric, D., Wu, K., 2021. Mixing performance and continuous production of nanomaterials in an advanced-flow reactor. Chem. Eng. J. 412, 128565 https://doi.org/10.1016/j.cej.2021.128565.

Zhang, T.B., Lu, Y.C., Luo, G.S., 2013. Iron phosphate prepared by coupling precipitation and aging: Morphology, crystal structure, and Cr(III) adsorption. Cryst. Growth Des. 13, 1099–1109. https://doi.org/10.1021/cg301441t.

Zhang, Z., Wang, K., Xu, C., Zhang, Y.U., Wu, W., Lu, C., Liu, W., Rao, Y., Jiang, C., Xu, C., Song, S., 2022. Ultrasound enhancing the mass transfer of droplet microreactor for the synthesis of $AgInS_2$ nanocrystals. Chem. Eng. J. 435, 134948 https://doi.org/10.1016/j.cej.2022.134948.

Zhang, L., Xie, W., Guo, S., Xia, X., Yang, S., 2023. Microflow precipitation of barium sulfate nanoparticles from mineral barium sulfide black ash. Chem. Eng. Process. 184, 109298 https://doi.org/10.1016/j.cep.2023.109298.